



Synergistic effect of manganese (II) phosphate & diamond nanoparticles in electrochemical sensors for reactive oxygen species determination in seminal plasma

Eva Pérez^a, Luis Vázquez^b, Carmen Quintana^a, María Dolores Petit-Domínguez^a, Elena Casero^a, Elías Blanco^{a,*}

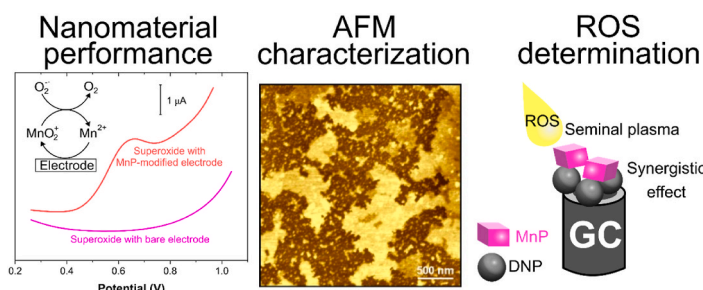
^a Departamento de Química Analítica y Análisis Instrumental, Facultad de Ciencias, c/ Francisco Tomás y Valiente, N°7, Campus de Excelencia de la Universidad Autónoma de Madrid, 28049, Madrid, Spain

^b Instituto de Ciencia de Materiales de Madrid (ICMM), CSIC, c/ Sor Juana Inés de la Cruz N°3, Campus de Excelencia de la Universidad Autónoma de Madrid, 28049, Madrid, Spain

HIGHLIGHTS

- Manganese (II) phosphate (MnP) synthesis by bottom-up solution chemistry.
- MnP shows catalysis towards ROS electroanalysis.
- Synergistic effects between MnP & 2D-ReS₂ or diamond nanoparticles.
- Diamond nanoparticles/MnP-based sensor allows ROS analysis in seminal plasma.

GRAPHICAL ABSTRACT



ARTICLE INFO

Handling Editor: Professor Chuck Henry

Keywords:

Manganese (II) phosphate nanomaterial
Diamond nanoparticles
Electrochemical sensor
Reactive oxygen species
Seminal plasma

ABSTRACT

In this work, we explore the ability of manganese (II) phosphate (MnP) as a catalytic element for the determination of reactive oxygen species (ROS) in seminal plasma, when MnP is employed as modifier of a glassy carbon electrode. The electrochemical response of the manganese (II) phosphate-modified electrode shows a wave at around +0.65 V due to the oxidation of Mn^{2+} to MnO_2^+ , which is clearly enhanced after addition of superoxide, the molecule considered as the mother of ROS. Once proved the suitability of manganese (II) phosphate as catalyst, we evaluate the effect of including a 0D (diamond nanoparticles) or a 2D (ReS_2) nanomaterial in the sensor design. The system consisting of manganese (II) phosphate and diamond nanoparticles yielded the largest improvement of the response. The morphological characterization of the sensor surface was performed by scanning electron microscopy and atomic force microscopy, while cyclic and differential pulse voltammetry were employed for the electrochemical characterization of the sensor. After optimizing the sensor construction, calibration procedures by chronoamperometry were performed, leading to a linear relation between peak intensity and the superoxide concentration in the range of $1.1 \cdot 10^{-4} \text{ M}$ – $1.0 \cdot 10^{-3} \text{ M}$ with a limit of detection of $3.2 \cdot 10^{-5} \text{ M}$. Seminal plasma samples were analysed by the standard addition method. Moreover, the analysis of samples fortified with superoxide at the μM level leads to recoveries of 95%.

* Corresponding author.

E-mail address: elias.blanco@uam.es (E. Blanco).

<https://doi.org/10.1016/j.aca.2023.341301>

Received 23 February 2023; Received in revised form 26 April 2023; Accepted 28 April 2023

Available online 29 April 2023

0003-2670/© 2023 The Authors. Published by Elsevier B.V. This is an open access article under the CC BY-NC-ND license (<http://creativecommons.org/licenses/by-nc-nd/4.0/>).

1. Introduction

Reactive oxygen species (ROS) are short-lived intermediates in the metabolism that have at least one oxygen atom. They are radicals or non-radical molecules characterized by their oxidizing power. Among them, we can mention superoxide ($O_2^{\cdot-}$), ozone (O_3), hydroxyl radical (OH^{\cdot}), hydrogen peroxide (H_2O_2) or hydroperoxides (R-O-O-H). ROS react with nucleic acids, proteins, lipids and carbohydrates. Their high concentration is linked to aging and several diseases such as cancer, cardiovascular pathologies, or neurodegenerative conditions. Furthermore, they have a role in the sperm fertilization ability [1–3].

Infertility is a World Health Organization (WHO)-recognised disease that is diagnosed when pregnancy is not achieved after one year or more of regular unprotected intercourse [4]. Global fertility rates and sperm count (concentration) have decreased, showing that the disease is spreading. Recent data indicate that nearly 50 million couples are affected every year, being the male factor the only responsible in 30% of these cases [3,4]. Several causes can be behind male infertility such as varicocele (elevated scrotal temperature), testicular cancer, lifestyle (alcohol consumption, smoking, obesity), or infections [2,4]. Male reproductive capacity is assessed by parameters such as sperm count, motility, and morphology, that are evaluated according to the WHO guidelines, through analyses called seminogram. With its reference ranges, it is still the gold standard tool for evaluating male infertility. However, there are men with normal seminal parameters who are infertile (case of 15–30% of all infertile couples) and, therefore, in these cases, the seminogram results cannot be used as a proof of infertility. In order to solve these issues, analysis of both sperm DNA fragmentation and ROS are also employed [3,4].

The “Oxygen Paradox” consists in that the oxygen required to follow an aerobic life produces ROS. Although these molecules are essential for normal cell functions, the condition of oxidative stress is achieved when an overproduction occurs and the antioxidant mechanism becomes overwhelmed [1]. In the case of sperm cells, ROS are involved in maturation, capacitation, hyperactivation, acrosome reaction, and fusion with the female gamete. The oxidative stress condition leads to both increased DNA fragmentation and membrane oxidation. DNA damage would cause poor embryogenesis and miscarriage, while membrane harms would produce effects such as poor motility or morphological abnormalities, which are parameters evaluated in the seminogram [1–3].

Although relatively unreactive, superoxide is considered the mother of ROS, and is produced: i) in the inner mitochondrial membrane between complex I and III of the electron transport chain, and ii) in the plasma membrane by NAD(P)H-oxidase [1,3]. To analyse ROS in seminal samples, the most recent WHO manual for assessment includes chemiluminescence and electrochemical techniques. Electroanalytical methods offer high sensitivity, requiring low-cost and easy-of-use equipment, which can be miniaturized and portable. In particular, the development of electrochemical sensors based on nanomaterials is of great interest to improve the performance towards the determination of compounds with biological and environmental interest [5–13]. In this sense, for the electrochemical analysis of superoxide, biosensors based on superoxide dismutase (SOD) are a good alternative because of their low detection limit and high selectivity [14]. However, their potential inactivation, by environmental conditions or by the measurement media, has caused that other options are being explored. Among them, we can mention the employment of nitrogen-doped hollow mesoporous carbon spheres as the only modifier of the electrode surface [15]. This nanomaterial is a promising alternative due to its high surface area, good electrical conductivity and high density of edge-plane-like surface defects that boost electronic transference. Many of the proposals for the superoxide electroanalysis in aqueous media include inorganic cations that allow the electron transference with the analyte, just like it occurs in the case of the SOD active centre and other biological elements used in superoxide biosensor development. Examples of strategies including

cations are a bidimensional metal-organic framework with copper [16], a copper complex with cysteine and gold nanoparticles [17], and the based-on manganese (II) phosphate $Mn_3(PO_4)_2$ (MnP). In this case, different alternatives for obtaining MnP have been explored such as mixing a Mn salt and tribasic phosphate [18], Mn(II) adsorbed on a zeolite in which the phosphate source comes from the measurement electrolyte [19], or the addition of Mn(II) over a melamine-phytic acid aggregate, where phosphate groups are included in the phytic acid molecule [20].

Besides the catalytic element, almost every MnP-based platform uses a component to facilitate the electronic transference such as porous laser-induced graphene [16], titanium carbide [18] or multi-walled carbon nanotubes [20]. Silicon carbide has been also used in a biosensor with SOD [14]. Detonation diamond nanoparticles (DNP) and transition metal dichalcogenides (TMD), mostly MoS_2 and WS_2 , are nanomaterials that have recently demonstrated their utility for the enhancement of the sensor properties when employed as electrode modifiers, for example for the analysis of food colourants [21] or herbicides [22]. However, they have never been used together with MnP for the development of ROS sensors. DNP and TMD exert favourable increases of electrical conductivity and surface area. DNP enhance the electrochemical response due to the overlapping of the surface unsaturated bonds orbitals, which results in discrete electronic states within the diamond band gap [23,24]. Respect to the more widespread use of MoS_2 , other TMD, such as ReS_2 , have been less employed, although the van der Waals forces that maintain the layers stacking are weaker, which leads to an easier obtention by liquid exfoliation. In addition, ReS_2 has higher surface area and more edge sites for possible catalytic phenomena [25,26].

The aim of this work is to explore the utility of manganese (II) phosphate, together with DNP and/or ReS_2 as elements for facilitating the electronic transference and the spread of MnP, as modifiers of glassy carbon electrodes (GCE) for the electroanalysis of ROS, expressed as superoxide concentration, in seminal samples. After the optimization of the sensor construction, the surface of the resulting sensor was characterized by scanning electron microscopy (SEM) and atomic force microscopy (AFM), and the calibration curve and the analytical parameters of the sensor were obtained. Finally, the sensor was applied in the ROS determination in real seminal plasma. To the best of our knowledge, this is the first time that an electrode modifier intended for the analysis of superoxide is evaluated towards seminal plasma analysis, unlike studies where the sensor applicability is verified by the superoxide release of stimulated cell cultures [15,16,18–20].

2. Experimental section

2.1. Materials

SkySpring Nanomaterials, Inc (Houston, Texas, USA) supplied the diamond nanoparticles with a nominal size of 4–15 nm and a carbon content of 55–75%, according to the supplier. Manganese (II) sulphate, sodium citrate dehydrate, and urea were obtained from Panreac Quimica SLU (Castellar del Vallès, Spain). Scharlab (Senmanat, Spain) provided ethanol, dimethyl sulfoxide, potassium chloride, phosphoric acid, sodium hydroxide, D(+)-glucose, D(–)-fructose, L(+)-lactic acid, potassium hydroxide and zinc chloride. Potassium superoxide, 18-crown-6, bovine serum albumin (BSA), rhenium disulphide and sodium phosphate tribasic were supplied by Sigma-Aldrich (St. Louis, Missouri, USA). Glassy carbon electrodes and Ag/AgCl/3 M KCl were obtained from CH Instruments, Inc (Austin, USA). A platinum wire was used as counter electrode. Before modification of GCE, 1 μ m-diamond paste supplied by Buehler (Lake Bluff, Illinois, USA) was used to polish them. All aqueous solutions were prepared with deionised water of resistivity not less than 18.2 M Ω cm.

2.2. Apparatus

An Autolab PGSTAT 302 N from Eco-Chemie (Utrecht, The Netherlands) was used to perform the electrochemical measurements.

The AFM data were obtained with two systems, namely a Nanoscope IIIa (Veeco, Plainview, New York, USA) and an Agilent Picoplus 5500 (Agilent, Santa Clara, California, USA) operating in the dynamic mode. For the topographic imaging, silicon cantilevers with nominal radius of 8 nm and constant force in the 1–5 N/m range (Bruker, Billerica, Massachusetts, USA) were employed. These images consisted of 512 x 512 pixels. The Agilent system was applied to perform single pass Kelvin Force Microscopy (KFM) imaging. For these measurements, Pt coated tips, model ANSCM-PT-20 (AppNano, Mountain View, California, USA), with a radius smaller than 40 nm, were used. In this mode, together with the topographic image, two more images are recorded. One registers the contact potential difference (CPD) whose changes are related to local variations of the surface potential. The other records the gradient of the tip-sample capacitance ($\partial C/\partial z$) whose changes are related to variations of the dielectric constant. In these cases, the images consisted of 1024 x 1024 pixels. Finally, the Magnetic Force Microscopy (MFM) measurements were done with the Nanoscope IIIa system (Veeco, Plainview, New York, USA) operating in the lift mode with a lift height of 35 nm. Co/Cr coated tips (MESP model, Bruker) were employed. In this case, in the scan registered in the lift mode, the phase contrast, $\Delta\phi$, is recorded.

Scanning Electron Microscopy (SEM) data were obtained with a FEI Nova NanoSEM (Thermo Fisher Scientific Inc., Waltham, Massachusetts, USA) operating at 15 keV and using the vCD detector.

X-ray Diffraction (XRD) measurements were performed using a Bruker (Billerica, Massachusetts, USA) D8 Advance diffractometer $\theta/2\theta$, equipped with a Cu K α 1 radiation ($\lambda = 1.54056 \text{ \AA}$), a primary Ge monochromator and Lynxeye XE-T Detector. Data were collected in the 2θ range from 10 to 70.

The pH of solutions was measured with a pH meter Metrohm C831 equipped with an Ag/AgCl reference electrode (Herisau, Switzerland). A Rotofix 32 A centrifuge (Hettich, Tuttlingen, Germany) and an ultrasonic bath Transonic 570/H (Elma, Singen, Germany) were employed for nanomaterials preparation.

2.3. Procedures

2.3.1. Synthesis of manganese phosphate suspension

Manganese sulphate and sodium phosphate tribasic solutions were prepared, independently. In a beaker, 17 μmol Mn(II) were added in 40 mL of water. A phosphate excess of 3 times the stoichiometrically needed (34 μmol) was added in 30 mL of water and this solution was poured, drop by drop, in the Mn(II) solution during 30 min approximately under magnetic stirring. Afterwards, the mixture was centrifuged at 4000 rpm 10 min and the solid was washed with water, process that was repeated 3 times. To end, 2 mL of water were added to the solid to obtain a suspension of 1 mg mL^{-1} [18].

2.3.2. Preparation of 2D- ReS_2 and DNP suspensions

We followed a liquid exfoliation procedure assisted by ultrasounds to obtain TMD nanosheets. It consists in weighting around 75 mg of the commercial substance and adding 10 mL of a mixture EtOH:H $_2$ O (45:55 v/v). In an ultrasounds bath, the mixture was treated for 2 h and then was aged for one day at 4 °C. Afterwards, it was centrifuged at 4000 rpm for 45 min. The supernatant was collected and kept at 4 °C when not in use [21,22]. On the other hand, commercial DNP were accurately weighted, water was added and the mixture (1 mg mL^{-1}) was sonicated for 15 min. The resulting suspension was stored at 4 °C.

2.3.3. Preparation of superoxide stock solutions

Around 135 mg of 18-crown-6 were weighted in a vial and dissolved in 3 mL of dimethyl sulfoxide. Next, this solution was added to an accurately weighted amount of potassium dioxide, around 18 mg, and

was bath-sonicated. The cyclic oligomer was employed to promote the dissolution of the superoxide salt. The resulting solution was transferred to a volumetric flask and diluted with dimethyl sulfoxide up to 5.00 mL [27]. This solution was daily prepared.

2.3.4. Electrode modification

Prior to its modification with any material, the GCE was polished with 1 μm diamond paste, sonicated in ethanol and water, and dried with a nitrogen stream. Next, it was modified with 6 μL of the corresponding stock suspension and allowed to dry at room temperature, either for a subsequent modification or for its use. The preparation of the stock suspensions of DNP, MnP and ReS_2 is described above. The evaluated sensor constructions were GCE/MnP, GCE/DNP, GCE/ ReS_2 , GCE/ ReS_2 /MnP, GCE/DNP/MnP, GCE/DNP/ ReS_2 /MnP, and GCE/ ReS_2 /DNP/MnP.

2.3.5. AFM and SEM samples preparation

For AFM and SEM measurements, the samples were prepared in SiO_2 surfaces by drop-casting of 10 μL of the corresponding nanomaterial suspension. For GCE/MnP, a 1:100 diluted suspension of MnP was employed for modification. For the system GCE/DNP/MnP, two different samples were prepared. In the first one, the stock suspensions of DNP (1 mg mL^{-1}) and MnP (1 mg mL^{-1}) were directly used for modification, i.e., at the same concentration employed for the electrochemical sensor. In the second one, a 1:100 diluted suspension of both MnP and DNP was employed. The diluted preparations were intended to avoid the generation of high rough surfaces, which hampers the AFM characterization.

2.3.6. Electrochemical measurements

0.1 M phosphate buffer pH 7 was used as electrolyte. Every potential quoted in this work is with respect to the Ag/AgCl/3 M KCl reference electrode. Differential pulse voltammetric (DPV) measurements were performed at a scan rate of 20 mV/s and applying pulses of 60 mV of amplitude. For the calibration procedures, the interference study and the sample analyses, we used chronoamperometry at +0.70 V with magnetically stirred solutions.

2.3.7. Human semen collection and sample preparation

A healthy man, who expressed consent for the sperm collection and analysis, participated in the study. After ejaculatory abstinence between 2 and 7 days, the sample was taken, allowed to liquefy for 30 min at room temperature and subjected to bath sonication. This treatment allows the superoxide release as otherwise the analyte cannot traverse cellular membranes. Finally, the sample was subjected to centrifugation (10 min at 1800 rpm), treatment that allows to obtain the plasma (supernatant) from the whole semen. The sample was preserved at 4 °C between analyses [28,29]. An aliquot of the sample was diluted 1:100 with electrolyte and analysed by the standard addition method. Moreover, an aliquot of the sample was fortified with superoxide to achieve a concentration of 10.5 mM to evaluate the recovery of the method.

3. Results and discussion

3.1. Evaluation of MnP as electrode modifier for superoxide detection

The literature about ROS determination remarks the need of modifying conventional electrode surfaces, such as the GCE used in this work, with nanomaterials because the unmodified electrodes do not respond to the analyte. It is observed by DPV that when the unmodified electrode, in phosphate buffer pH 7, is in presence of superoxide (Fig. 1, curve b) no peak develops. Rather, a current increment respect to the electrolyte (curve a) occurs, which is maximum for potentials higher than 0.9 V. This high potential value would hamper the analysis as other electroactive compounds can be in real samples. The voltammogram obtained with the GCE modified with the catalyst $\text{Mn}_3(\text{PO}_4)_2$ (GCE/MnP) just in

electrolyte (Fig. 1, curve c) shows a wave at around 0.65 V due to the oxidation of Mn^{2+} to MnO_2^+ according to the literature [19,20]. The addition of superoxide makes this wave higher in intensity (curve d), demonstrating the suitability of MnP as catalyst for the oxidation of the analyte. As can be observed in the inset of Fig. 1, the increase of intensity obtained when O_2^- is added can be explained as follows: i) MnO_2^+ is produced in the anodic scan as a consequence of the electrochemical oxidation of Mn^{2+} (MnP), ii) as MnO_2^+ is being produced, it oxidizes O_2^- , process that allows the regeneration of Mn^{2+} [19,20].

Scan e of Fig. 1 is the result of the subtraction of the voltammogram recorded just in electrolyte (scan c) from that registered in presence of superoxide (scan d). In order to make the results clearer, hereafter the displayed voltammograms are the result of this subtraction because the presence of MnP always results in the arise of this wave without superoxide.

3.2. Optimization of the sensor construction

Once the catalytic effect of MnP for O_2^- detection had been verified, we proceeded to optimize the sensor construction in order to obtain an enhanced response. First, we studied how the concentration of MnP employed for modifying the electrode surface could change the signal. In Fig. 2, we see the response employing sensors prepared by drop-casting of 6 μL of MnP suspensions with concentrations ranging from 0.05 mg mL^{-1} to 4 mg mL^{-1} . As can be observed, the best response is obtained for a concentration of 1 mg mL^{-1} , which was used for further studies.

Next, we evaluated the effect of including a 0D (DNP) or a 2D (ReS_2) nanomaterial in the sensor design because of the excellent properties they confer. DNP are known for increasing electric conductivity and conferring catalysis. ReS_2 can improve the developed platform in base of its high surface-to-volume ratio that can lead to a better MnP accommodation. Before combining MnP with these nanomaterials, we checked the response of GCE/DNP and GCE/ ReS_2 , in the presence and in the absence of superoxide, and no significant differences were observed (Fig. S1).

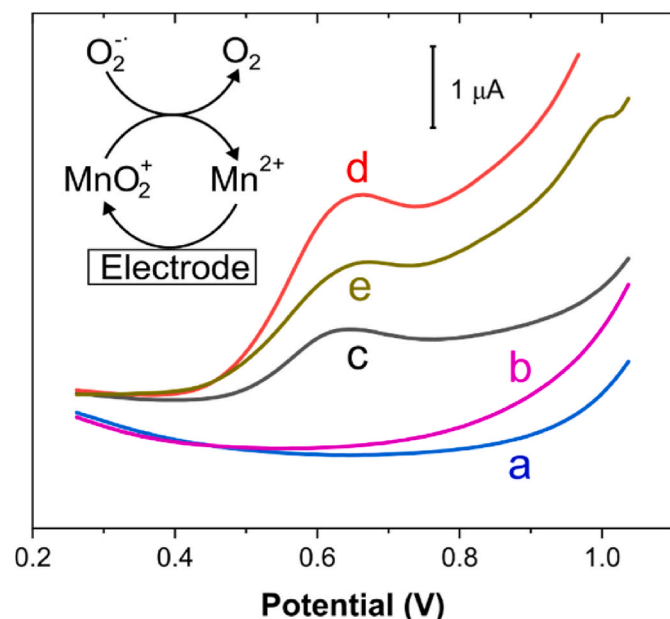


Fig. 1. DPV recorded with bare GCE (a and b) and with GCE/MnP (c, d). Measurements a and c were recorded without analyte, and b and d in presence of 1.00 mM O_2^- . Curve e is the subtraction of the DPV registered in presence of analyte (curve d) minus the recorded just in electrolyte (curve c). 0.1 M phosphate buffer pH 7 was used as electrolyte. Scan rate of 20 mV/s and amplitude of 60 mV. Inset: Oxidation process of O_2^- catalysed by $\text{Mn}^{2+}/\text{MnO}_2^+$ and regeneration.

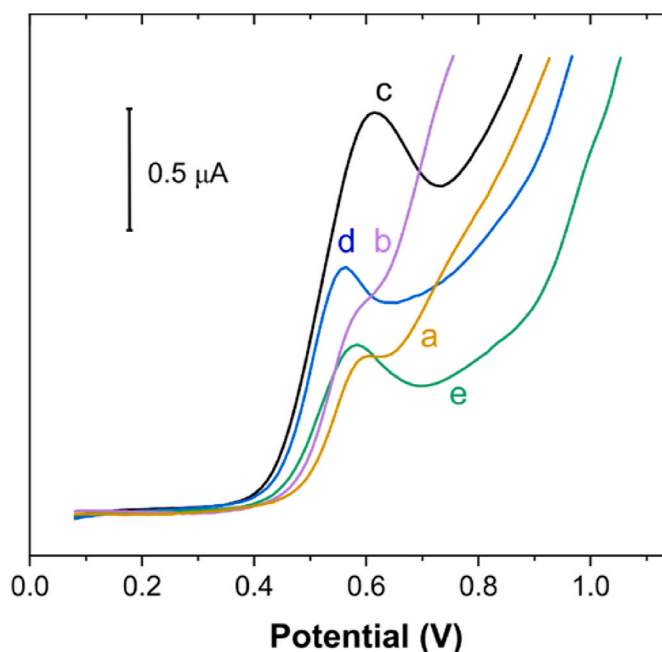


Fig. 2. DPV obtained for 1.00 mM O_2^- , employing sensors prepared from suspensions with different MnP concentrations: 0.05 mg mL^{-1} (a), 0.1 mg mL^{-1} (b), 1 mg mL^{-1} (c), 2 mg mL^{-1} (d), and 4 mg mL^{-1} (e). Electrolyte: 0.1 M phosphate buffer pH 7. Scan rate 20 mV/s and amplitude 60 mV.

However, the sequential modification with a first layer of the ReS_2 suspension and then with MnP (GCE/ ReS_2 /MnP) resulted in a signal increase of 0.43 μA with respect to MnP as the only modifier (Fig. 3, voltammograms a and b) without shift of the peak potential. For GCE/DNP/MnP (curve c), a much higher current increase is observed, specifically 1.28 μA , with a small shift to lower potentials. Therefore, the inclusion of a first layer of DNP or ReS_2 improves the signal observed just with MnP. This enhancement is not due to the response to the analyte of these materials (see Fig. S1) but to a synergistic effect where the hybrid material causes better responses than the sum of the individual signals. We then studied whether modifications including the three nanomaterials, DNP, ReS_2 and MnP, could yield better responses than those already found. Although better than GCE/ ReS_2 /MnP (Fig. 3, curve b), the modifications including the three nanomaterials (GCE/DNP/ ReS_2 /MnP and GCE/ ReS_2 /DNP/MnP, shown in Fig. 3 curves d and e, respectively) display lower currents than the simpler modification GCE/DNP/MnP of the voltammogram c. Therefore, GCE/DNP/MnP is chosen for further experiments.

The study of the electrochemical mechanism was performed by cyclic voltammetry changing the scan rate between 20 and 500 mV/s. After the subtraction of the measurements with superoxide minus that performed without it for each rate, the obtained voltammograms are shown in Fig. S2A where, as expected, both anodic and cathodic waves increased their currents as the scan rate was increased.

The current intensity of the anodic process, in which we are interested in for the analyte quantification, was monitored and the plot versus the square root of the scan rate appears in Fig. S2B. The excellent fit in the whole scanned range suggests a diffusive electrochemical process.

3.3. AFM characterization of the sensor

Before presenting the AFM characterization of the DNP/MnP surface, it is necessary to analyse the MnP system. Previously, we characterized the as-synthesized MnP by XRD (Fig. S3). The main peaks at $\sim 10.4^\circ$, $\sim 12.9^\circ$, and $\sim 34.4^\circ$ correspond to the standard pattern of $\text{Mn}_3(\text{PO}_4)_2 \cdot 3\text{H}_2\text{O}$ (see red spectrum). The peak close to 10.4° is due to the

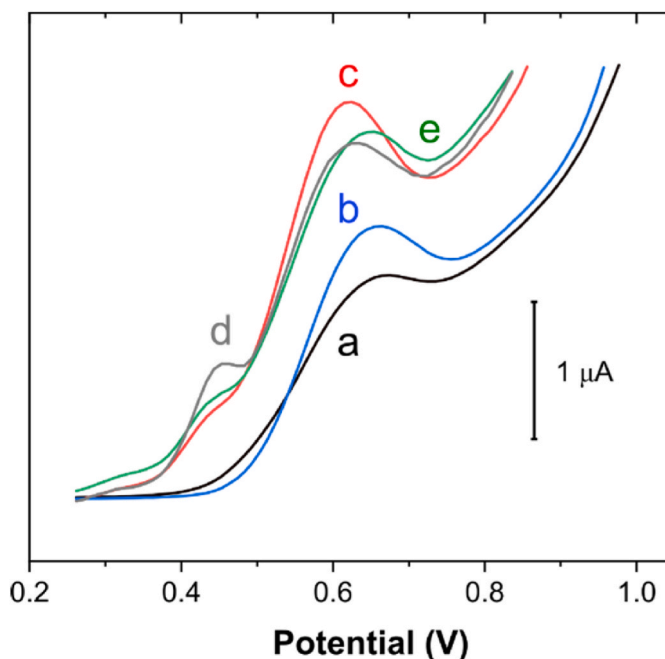


Fig. 3. DPV (electrolyte signal subtracted) obtained with 1.00 mM O_2^- and different modified electrodes: GCE/MnP (a), GCE/ReS₂/MnP (b), GCE/DNP/MnP (c), GCE/DNP/ReS₂/MnP (d), and GCE/ReS₂/DNP/MnP (e). Electrolyte: 0.1 M phosphate buffer pH 7. Scan rate 20 mV/s and amplitude 60 mV.

existence of a layered structure [30]. A next step consisted in analysing the MnP deposits on Si by SEM and AFM (see preparation conditions above). As Fig. 4A shows over the bright Si surface, two-dimensional (2D) darker structures are found together with bright three-dimensional ones. These 2D features were also imaged by AFM (Fig. 4B–D). These measurements confirmed that there are two-dimensional flakes on the flat Si surface. This finding agrees with previous reports [31,32]. In some locations, thicker regions, which appear with a brighter contrast, can be observed. This is clearly seen in

the surface profile shown in Fig. 4C corresponding to the long line in Fig. 4B. The height of the thinnest flakes is obtained from the height distribution of Fig. 4B, which is displayed in Fig. 4D (note that the x-axis corresponds to the height levels). Two main peaks appear, that at x-axis value close to zero corresponds to the Si surface meanwhile the one close to $x = 2$ nm comes from the thinnest flakes. Thus, the distance along the x-axis between these two peaks corresponds to the thickness of the thinnest layer, which results to be 2–2.5 nm, which is lower than the layer thickness close to 3.5 nm reported previously on a similar system but with different preparation procedure (see Supporting Information of [32]). Furthermore, there is also a shoulder at $x \sim 4$ nm, which is due to the thicker structures. The distance along the x-axis between the middle peak and this one, ~ 2.3 nm, is similar to that of the thinnest flakes, suggesting that these regions could come from the stacking of two thin flakes. The image in Fig. 4B and the plot of Fig. 4C, show that on top of the Si surface and that of the MnP flakes there are tiny rounded structures that should come from the MnP deposit. Their height lies in the 2–3 nm range.

Previously, the magnetic properties of MnP structures had been highlighted [31]. Accordingly, we attempted to characterize the MnP flakes by MFM. Fig. S4 shows the topographical image together with the corresponding MFM image. The MnP flakes are clearly observed. The thinner flakes have a height close to 2.3 nm whereas the thicker ones show values close to 4.1 nm. The corresponding MFM image shows a clear brighter contrast on top of the MnP flakes, about 0.4° higher than that of the surrounding substrate. It is worth noting that there are a few rounded high structures on the topographic image that do not show enhanced MFM contrast, which allows to discard topographical contamination on the MFM signal.

Fig. 5A shows an AFM image of the DNP/MnP sample. One flake is observed and the corresponding surface profile across its surface is shown in Fig. 5B. Its thickness is in the 2–3 nm range. Scattered on the silicon and flake surfaces, round particles and aggregates are observed. In principle, due to the preparation sequence, those structures found on the MnP flakes should correspond to the MnP deposit. However, as shown in Fig. 5A, the MnP flakes are not complete since they present many holes. In many of these holes are found rounded structures that likely correspond to DNP structures. Similar structures are found outside

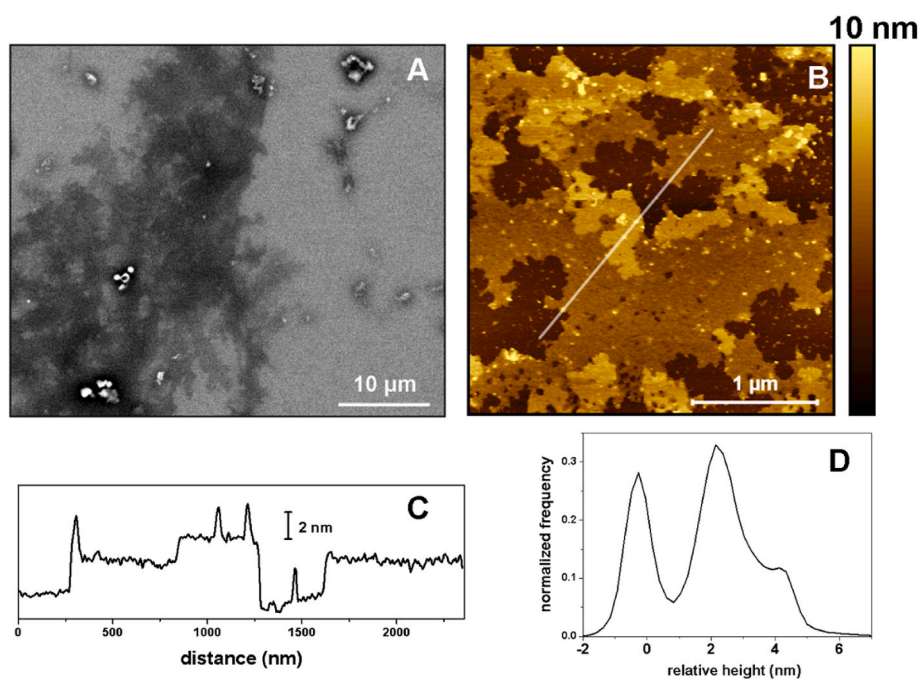


Fig. 4. A) SEM image of the 1:100 diluted suspension of MnP deposited on Si. B) AFM of the same MnP deposit on Si surface. C) Surface profile along the long line depicted in B. D) Height distribution of 4B.

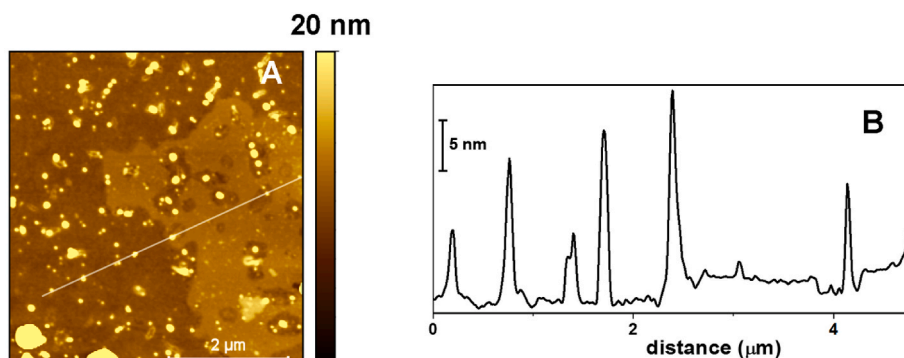


Fig. 5. A) AFM of the DNP/MnP deposit. B) Surface profile along the long line depicted in A.

of the MnP flakes. The smallest DNP structures have heights in the 4–15 nm range (see profile). Other larger structures are due to the tendency of the DNP to aggregate.

Fig. 6A, C, and 6E show the three-dimensional representation of the topographic (6A), CPD (6C) and gradient of the capacitance (6E) images taken simultaneously on other zone of the DNP/MnP sample with less DNP particles (they appear as small bright rounded structures). Three large MnP flakes are imaged, together with smaller ones. As noted, some DNP rounded structures are found in the MnP flake and on the silicon surface.

The average thickness of the flakes can be obtained from the height distribution plot (Fig. 6B) as two clear peaks appear. The horizontal distance between them, i.e. the average thickness, corresponds to 2.7

nm. The flakes, even the smallest ones, yield a clear CPD contrast with respect to that of the silicon, indicating that are from other material (Fig. 6C). The measured value on top of the flakes is 80 mV higher than that obtained on the substrate. In fact, the height distribution of the CPD image also shows two peaks (Fig. 6D) evidencing the clear CPD contrast between the signals of the flakes and the silicon. In the case of the gradient of the capacitance (Fig. 6E) the contrast between these two regions is rather small, around 15 mV, which is just a bit larger than the noise level. Notwithstanding, it is clear that the flakes show a lower signal that the surrounding silicon. Furthermore, a detailed analysis (not shown) shows that the DNP structures have an even lower signal level than the flakes.

Finally, Fig. S5A shows two characteristic SEM images of the DNP/

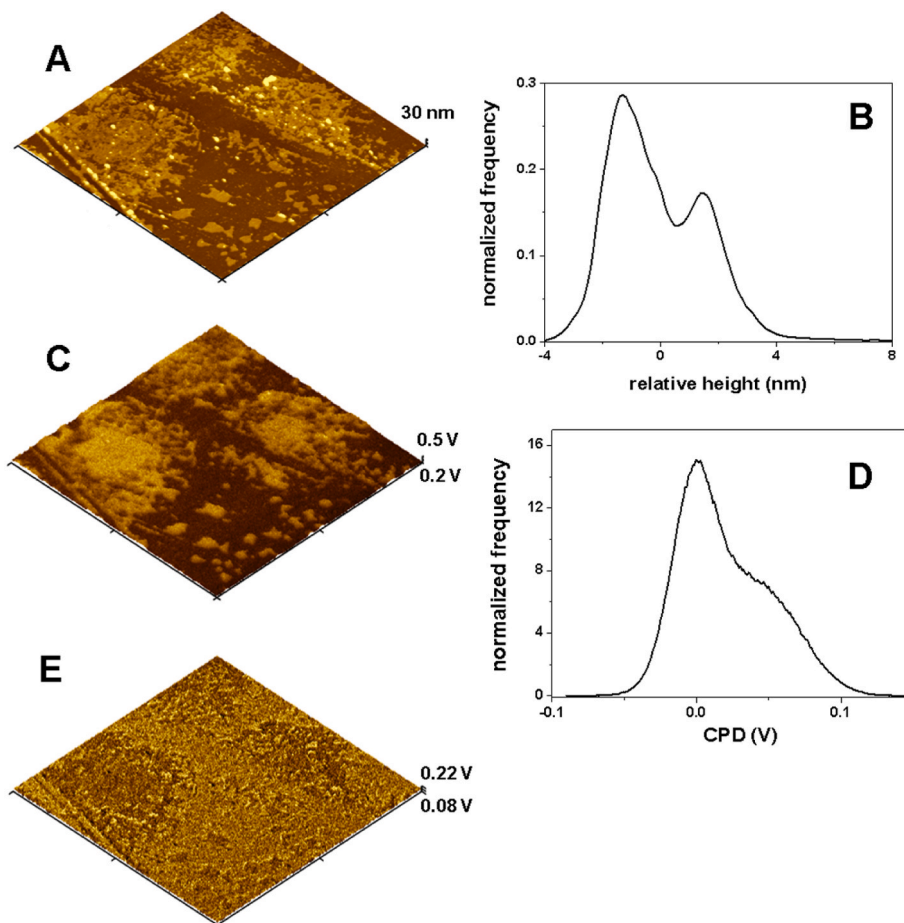


Fig. 6. A) $8 \times 8 \mu\text{m}^2$ 3D topographic AFM of the DNP/MnP deposit. B) Height distribution of the image in A. C) CPD image of the same area of A. D) Height distribution of the image in C. E) Gradient of the capacitance image of the same area of A.

MnP sample deposited on silicon at the same concentration than that used for the sensing device. Flowerlike round aggregates are observed. They can be ascribed to MnP aggregates according to previous reports [32,33]. Due to the rough morphology, the AFM imaging of this sample becomes rather difficult. Nevertheless, it was possible to obtain images of reduced size as those displayed in Figs. S5B and S5C in which the surface roughness is ~ 300 nm. The surface is formed by flat flakes stacked at different tilting angles surrounded by large aggregates of DNP structures. This can be better appreciated in the three-dimensional image shown in Fig. S5C. Here, a large flake strip is imaged at the centre, with aggregates of rounded structures around. The surface of the flake is rather smooth, with a roughness in the 1–2 nm range, although scattered MnP isolated nanostructures are also found on it.

3.4. Influence of the superoxide concentration in the analytical signal. Analytical data

Once the sensor construction was optimized and morphologically characterized, the calibration procedure by chronoamperometry at $+0.70$ V was performed by successively adding volumes of a superoxide standard solution to an electrolyte solution under stirring. With each addition, the current increased as shown in Fig. 7A. The corresponding representation of the current intensity in each plateau versus the concentration is shown in Fig. 7B. The calibration was linear between 0.11 and 1.00 mM according to equation $I (\mu\text{A}) = (4.7 \pm 0.2) [\text{O}_2^-] (\text{mM}) + (0.10 \pm 0.04)$ with $r = 0.997$ ($n = 3$). Higher concentrations resulted also in current increase, but the linearity was lost. The limits of detection ($3\sigma/\text{slope}$) and quantification ($10\sigma/\text{slope}$) were established in $3.2 \cdot 10^{-5}$ and $1.1 \cdot 10^{-4}$ M, respectively.

The precision and accuracy were studied at four concentration levels, and the corresponding results appear in Table 1, where precisions lower than 4.3% of RSD and accuracies lower than 6.8% are obtained. Concerning the storage stability, the sensor retained 95% of their initial response after a period of two weeks, indicating a good stability. Concerning the comparison with other works that have superoxide as the analyte of interest, several platforms can be found, such as those based on the employment of the 2D metal organic framework ELM-12 [16], nitrogen-doped hollow mesoporous carbon spheres [15], or on a nanocomposite of gold nanoparticles and a complex Cu(II)–cysteine [17]. With these platforms, linear concentration ranges like the reported here were achieved. As seen below in the section of the analysis of real sperm plasma, the obtained values are enough for the ROS electroanalysis in seminal samples.

As seminal plasma (sample without cells) can be viewed as a complex sample considering the number of compounds it has [34], a study of interferences was performed by adding each of these compounds sequentially to a solution containing a superoxide concentration of 0.5 mM. As can be seen in Fig. S6, the analyte addition gave rise to an

Table 1

Accuracy (E_r , %) and precision (reproducibility as RSD, %) values calculated for superoxide determination with the GC/DNP/MnP electrochemical sensor ($n = 3$).

$[\text{O}_2^-]$ standard (mM)	$[\text{O}_2^-]$ found (mM)	RSD (%)	E_r (%)
0.199	0.204	2.9	2.5
0.500	0.534	1.3	6.8
0.700	0.732	2.1	4.6
1.00	0.951	4.3	4.9

important current increase. Meanwhile, the ones of KCl, KOH, fructose, glucose, lactate, urea, BSA, and ZnCl_2 did not change the signal upon their addition. It is just observed a small signal fluctuation because of the solution stirring, slight changes that are also observed in Fig. 7A. However, the sodium citrate addition of 0.3 mM led to an increment of 10%

3.5. Analysis of real sperm plasma

Once the sample was pretreated and diluted with supporting electrolyte as specified in the experimental section, the standard addition method was followed and the chronoamperometric current was recorded at $+0.70$ V. As can be seen in Fig. 8A, the signal increased after each superoxide addition.

In Fig. 8B, the current intensity for each plateau of the chronoamperogram versus the concentration of standard added is presented. Fig. 8B also shows the fit with equation $I (\mu\text{A}) = (2.4 \pm 0.2) [\text{O}_2^-] (\text{mM}) + (1.2 \pm 0.1)$ with $r = 0.997$ ($n = 3$). After the corresponding extrapolation, the average concentration calculated is 0.48 ± 0.01 mM in the measured solution, which results in a concentration of 48 mM in the sample. The need of using the addition standard method instead of the external calibration was checked by comparing the slopes by the t -test. The t_{calc} was 1.69 while t_{tab} (4, 0.95) is equal to 2.78. Therefore, as the slopes are significantly different, the standard addition methodology has to be followed.

Furthermore, the real sample used in this work was also subjected to fortification and, once diluted 1:100, the added concentration of superoxide was 0.105 mM. The standard addition procedure was applied and we found that the plot of current in each plateau of the chronoamperometric signal versus added concentration fitted well to the linear equation $I (\mu\text{A}) = (2.4 \pm 0.2) [\text{O}_2^-] (\text{mM}) + (1.4 \pm 0.1)$ with $r = 0.997$ ($n = 3$). After extrapolation, the found concentration is 0.58 ± 0.02 mM. Taking into account the found concentration in the undoped sample, a recovery of 95% is obtained.

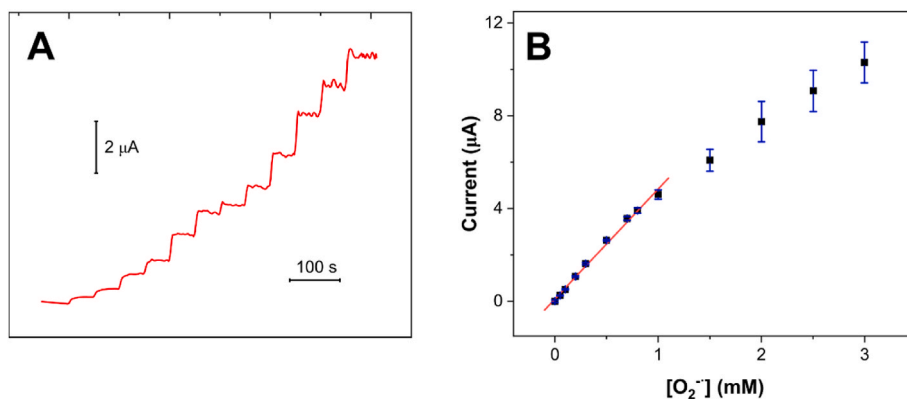


Fig. 7. A) Chronoamperogram obtained with GCE/DNP/MnP at $+0.70$ V in 0.1 M phosphate buffer pH 7 for successive additions of superoxide (0.05, 0.1, 0.2, 0.3, 0.5, 0.7, 0.8, 1.0, 1.5, 2.0, 2.5 and 3.0 mM). B) Corresponding calibration plot and linear fit. Error bars are plotted when they are larger than the symbol size.

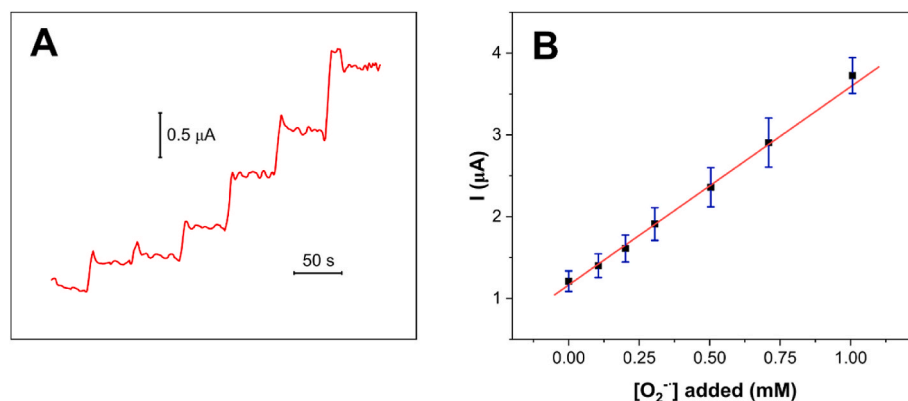


Fig. 8. A) Chronoamperogram obtained with GCE/DNP/MnP at +0.70 V with the real seminal sample diluted 1:100 in 0.1 M phosphate buffer pH 7 before and after successive additions of superoxide (0.1, 0.2, 0.3, 0.5, 0.7 and 1.0 mM). B) Corresponding calibration plot.

4. Conclusions

We have developed an electrochemical sensor based on the modification of a glassy carbon electrode with manganese (II) phosphate and diamond nanoparticles for reactive oxygen species determination. In the presence of superoxide, the synergistic effect between MnP and DNP leads to an enhanced intensity of the wave appearing at +0.65 V ascribed to the Mn oxidation. The morphology observed by AFM for the DNP/MnP sample deposited on silicon at the same concentration than that used for the sensing device is characterized by flat flakes stacked at different tilting angles together with large aggregates of DNP structures, which leads to a surface roughness around 300 nm. From the calibration performed by chronoamperometry, a linear relation between peak intensity and the ROS concentration, expressed as superoxide, in the range of $1.1 \cdot 10^{-4} \text{ M} - 1.0 \cdot 10^{-3} \text{ M}$ is found. Moreover, a limit of detection of $3.2 \cdot 10^{-5} \text{ M}$, a RSD lower than 4.3% and E_r lower than 6.8% are obtained. The sensor applicability to determine superoxide in real semen samples has been proved with a recovery of 95% for fortified samples at the μM level. To the best of our knowledge, sensors based on DNP and MnP had never been employed for determining ROS in real seminal plasma samples.

CRedit authorship contribution statement

Eva Pérez: Investigation, Validation, Writing – review & editing. **Luis Vázquez:** Methodology, Investigation, Visualization, Writing – original draft, Writing – review & editing. **Carmen Quintana:** Conceptualization, Methodology, Supervision, Writing – review & editing, Project administration, Funding acquisition. **María Dolores Petit-Domínguez:** Conceptualization, Methodology, Supervision, Writing – review & editing, Project administration, Funding acquisition. **Elena Casero:** Conceptualization, Methodology, Supervision, Writing – original draft, Writing – review & editing, Project administration, Funding acquisition. **Elías Blanco:** Conceptualization, Methodology, Supervision, Visualization, Writing – original draft, Writing – review & editing.

Declaration of competing interest

The authors declare that they have no known competing financial interests or personal relationships that could have appeared to influence the work reported in this paper.

Data availability

Data will be made available on request.

Acknowledgment

The authors acknowledge financial support from projects PID2020-113142RB-C21 and PID2020-113142RB-C22 and TED2021-129416A-I00 funded by MCIN/AEI/10.13039/501100011033 and P2018/NMT-4349 (TRANSNANOAVANSENS-CM) funded by the Comunidad Autónoma de Madrid. We thank I. Ballesteros for the SEM measurements and Noemí González Díaz from the Interdepartmental Research Service (SIDI) of the Universidad Autónoma de Madrid for the XRD measurements.

Appendix A. Supplementary data

Supplementary data to this article can be found online at <https://doi.org/10.1016/j.aca.2023.341301>.

References

- [1] J. Gosálvez, E. Tvrdá, A. Agarwal, Free radical and superoxide reactivity detection in semen quality assessment: past, present, and future, *J. Assist. Reprod. Genet.* 34 (2017) 697–707, <https://doi.org/10.1007/s10815-017-0912-8>.
- [2] K. Tremellen, Oxidative stress and male infertility—a clinical perspective, *Hum. Reprod. Update* 14 (2008) 243–258, <https://doi.org/10.1093/humupd/dmn004>.
- [3] P.E. Castleton, J.C. Deluao, D.J. Sharkey, N.O. McPherson, Measuring reactive oxygen species in semen for male preconception care: a scientist perspective, *Antioxidants* 11 (2022) 1–23, <https://doi.org/10.3390/antiox11020264>.
- [4] S. Minhas, C. Bettocchi, L. Boeri, P. Capogrosso, J. Carvalho, N.C. Gilesiz, A. Cocci, G. Corona, K. Dimitropoulos, M. Gül, G. Hatzichristodoulou, T.H. Jones, A. Kadioglu, J.I. Martínez Salamanca, U. Milenkovic, V. Modgil, G.I. Russo, E. C. Serefoglu, T. Tharakan, P. Verze, A. Salonia, European association of urology guidelines on male sexual and reproductive Health: 2021 update on male infertility, *Eur. Urol.* 80 (2021) 603–620, <https://doi.org/10.1016/j.eururo.2021.08.014>.
- [5] H. Beitollahi, S. Tajik, M.R. Aflatoonian, A. Makarem, Glutathione detection at carbon paste electrode modified with ethyl 2-(4-ferrocenyl-1,2,3-triazol-1-yl) acetate, *ZnFe₂O₄ nano-particles and ionic liquid*, *J. Electrochem. Sci. Eng.* 12 (2022) 209–217, <https://doi.org/10.5599/jese.1230>.
- [6] P. Mohammadzadeh Jahani, H. Beitollahi, A. Di Bartolomeo, A voltammetric sensor for the determination of hydroxylamine using a polypyrrole nanotubes-modified electrode, *Appl. Sci.* 12 (2022) 7485, <https://doi.org/10.3390/app12157485>.
- [7] H. Beitollahi, F. Garkani Nejad, S. Tajik, A. Di Bartolomeo, Screen-Printed graphite electrode modified with graphene- Co_3O_4 nanocomposite: voltammetric assay of morphine in the presence of diclofenac in pharmaceutical and biological samples, *Nanomaterials* 12 (2022) 3454, <https://doi.org/10.3390/nano12193454>.
- [8] P.M. Jahani, H. Beitollahi, F.G. Nejad, Z. Dourandish, A. Di Bartolomeo, Screen-printed graphite electrode modified with Co_3O_4 nanoparticles and 2D graphitic carbon nitride as an effective electrochemical sensor for 4-aminophenol detection, *Nanotechnology* 33 (2022), 395702, <https://doi.org/10.1088/1361-6528/ac779f>.
- [9] H. Beitollahi, S. Tajik, M.R. Aflatoonian, A. Makarem, A sensitive Cu(salophen) modified screen-printed electrode for simultaneous determination of dopamine and uric acid, *J. Electrochem. Sci. Eng.* 12 (2022) 199–208, <https://doi.org/10.5599/jese.1231>.
- [10] H. Moradpour, H. Beitollahi, Simultaneous electrochemical sensing of dopamine, ascorbic acid, and uric acid using nitrogen-doped graphene sheet-modified glassy carbon electrode, *Chimia* 8 (2022) 50, <https://doi.org/10.3390/ch8040050>.

- [11] H. Beitollahi, S. Tajik, A. Di Bartolomeo, Application of MnO₂ nanorod-ionic liquid modified carbon paste electrode for the voltammetric determination of sulfanilamide, *Micromachines* 13 (2022) 598, <https://doi.org/10.3390/mi13040598>.
- [12] M. Roostaee, H. Beitollahi, I. Sheikhshoae, Simultaneous determination of dopamine and uric acid in real samples using a voltammetric nanosensor based on Co-MOF, graphene oxide, and 1-Methyl-3-butylimidazolium bromide, *Micromachines* 13 (2022) 1834, <https://doi.org/10.3390/mi13111834>.
- [13] S. Tajik, Z. Dourandish, F. Garkani Nejad, H. Beitollahi, P.M. Jahani, A. Di Bartolomeo, Transition metal dichalcogenides: synthesis and use in the development of electrochemical sensors and biosensors, *Biosens. Bioelectron.* 216 (2022), 114674, <https://doi.org/10.1016/j.bios.2022.114674>.
- [14] H.A. Rafiee-Pour, A. Noorbakhsh, A. Salimi, H. Ghourchian, Sensitive superoxide biosensor based on silicon carbide nanoparticles, *Electroanalysis* 22 (2010) 1599–1606, <https://doi.org/10.1002/elan.200900577>.
- [15] L. Liu, H. Zhao, L. Shi, M. Lan, H. Zhang, C. Yu, Enzyme- and metal-free electrochemical sensor for highly sensitive superoxide anion detection based on nitrogen doped hollow mesoporous carbon spheres, *Electrochim. Acta* 227 (2017) 69–76, <https://doi.org/10.1016/j.electacta.2016.12.182>.
- [16] Q. Qiu, H. Chen, Z. You, Y. Feng, X. Wang, Y. Wang, Y. Ying, Shear exfoliated metal-organic framework nanosheet-enabled flexible sensor for real-time monitoring of superoxide anion, *ACS Appl. Mater. Interfaces* 12 (2020) 5429–5436, <https://doi.org/10.1021/acsami.9b17659>.
- [17] F. Dashtestani, H. Ghourchian, K. Eskandari, H.A. Rafiee-Pour, A superoxide dismutase mimic nanocomposite for amperometric sensing of superoxide anions, *Microchim. Acta* 182 (2015) 1045–1053, <https://doi.org/10.1007/s00604-014-1424-1>.
- [18] J. Zheng, B. Wang, Y. Jin, B. Weng, J. Chen, Nanostructured MXene-based biomimetic enzymes for amperometric detection of superoxide anions from HepG2 cells, *Microchim. Acta* 186 (2019) 95, <https://doi.org/10.1007/s00604-018-3220-9>.
- [19] J. Zhou, Y. Luo, A. Zhu, Y. Liu, Z. Zhu, Y. Tian, A reliable and durable approach for real-time determination of cellular superoxide anion based on biomimetic superoxide dismutase stabilized by a zeolite, *Analyst* 136 (2011) 1594–1598, <https://doi.org/10.1039/c0an00690d>.
- [20] X. Cai, L. Shi, W. Sun, H. Zhao, H. Li, H. He, M. Lan, A facile way to fabricate manganese phosphate self-assembled carbon networks as efficient electrochemical catalysts for real-time monitoring of superoxide anions released from HepG2 cells, *Biosens. Bioelectron.* 102 (2018) 171–178, <https://doi.org/10.1016/j.bios.2017.11.020>.
- [21] E. Blanco, L. Arias, L. Vázquez, M. del Pozo, L. Sánchez, M.D. Petit-Domínguez, C. Quintana, E. Casero, Sensor based on diamond nanoparticles and WS₂ for ponceau 4R and tartrazine determination: influence of green solvents employed for WS₂ exfoliation, *FlatChem* 23 (2020), 100185, <https://doi.org/10.1016/j.flatc.2020.100185>.
- [22] E. Blanco, L. Rocha, M. del Pozo, L. Vázquez, M.D. Petit-Domínguez, E. Casero, C. Quintana, A supramolecular hybrid sensor based on cucurbit[8]uril, 2D-molibdenum disulphide and diamond nanoparticles towards methyl viologen analysis, *Anal. Chim. Acta* 1182 (2021), 338940, <https://doi.org/10.1016/j.aca.2021.338940>.
- [23] K.B. Holt, Undoped diamond nanoparticles: origins of surface redox chemistry, *Phys. Chem. Chem. Phys.* 12 (2010) 2048–2058, <https://doi.org/10.1039/b920075d>.
- [24] T.S. Varley, M. Hirani, G. Harrison, K.B. Holt, Nanodiamond surface redox chemistry: influence of physicochemical properties on catalytic processes, *Faraday Discuss* 172 (2014) 349–364, <https://doi.org/10.1039/c4fd00041b>.
- [25] M.B. Askari, P. Salarizadeh, Ultra-small ReS₂ nanoparticles hybridized with rGO as cathode and anode catalysts towards hydrogen evolution reaction and methanol electro-oxidation for DMFC in acidic and alkaline media, *Synth. Met.* 256 (2019), 116131, <https://doi.org/10.1016/j.synthmet.2019.116131>.
- [26] Y. Liu, H. Li, J. Li, X. Ma, Z. Cui, D. Gao, Z. Tang, Fluorination activates the basal plane HER activity of ReS₂: a combined experimental and theoretical study, *J. Mater. Chem. A* 9 (2021) 14451–14458, <https://doi.org/10.1039/d1ta03258e>.
- [27] X. Cai, K. Chen, Z. Wang, W. Sun, H. Zhao, H. Zhang, H. Chen, M. Lan, Fabricating carbon-nanotubes-based porous foam for superoxide electrochemical sensing through one-step hydrothermal process induced by phytic acid, *Anal. Chim. Acta* 1038 (2018) 132–139, <https://doi.org/10.1016/j.aca.2018.07.014>.
- [28] E. Blanco, L. Vázquez, M. del Pozo, R. Roy, M.D. Petit-Domínguez, C. Quintana, E. Casero, Evaluation of oxidative stress: nanoparticle-based electrochemical sensors for hydrogen peroxide determination in human semen samples, *Bioelectrochemistry* 135 (2020), 107581, <https://doi.org/10.1016/j.bioelechem.2020.107581>.
- [29] F. Lanzafame, S. La Vignera, E. Vicari, A.E. Calogero, Oxidative stress and medical antioxidant treatment in male infertility, *Reprod. Biomed. Online* 19 (2009) 638–659, <https://doi.org/10.1016/j.rbmo.2009.09.014>.
- [30] Y.H. Dai, L. Bin Kong, K. Yan, M. Shi, Y.C. Luo, L. Kang, Facile fabrication of manganese phosphate nanosheets for supercapacitor applications, *Ionics* 22 (2016) 1461–1469, <https://doi.org/10.1007/s11581-016-1652-y>.
- [31] C.V.K. Sharma, C.C. Chusuei, R. Clérac, T. Möller, K.R. Dunbar, A. Clearfield, Magnetic property studies of manganese-phosphate complexes, *Inorg. Chem.* 42 (2003) 8300–8308, <https://doi.org/10.1021/ic0300520>.
- [32] H. Liu, X. Gao, X. Yao, M. Chen, G. Zhou, J. Qi, X. Zhao, W. Wang, W. Zhang, R. Cao, Manganese(II) phosphate nanosheet assembly with native out-of-plane Mn centres for electrocatalytic water oxidation, *Chem. Sci.* 10 (2019) 191–197, <https://doi.org/10.1039/C8SC03764G>.
- [33] K. Jin, J. Park, J. Lee, K.D. Yang, G.K. Pradhan, U. Sim, D. Jeong, H.L. Jang, S. Park, D. Kim, N.E. Sung, S.H. Kim, S. Han, K.T. Nam, Hydrated manganese(II) phosphate (Mn₃(PO₄)₂·3H₂O) as a water oxidation catalyst, *J. Am. Chem. Soc.* 136 (2014) 7435–7443, <https://doi.org/10.1021/ja5026529>.
- [34] D.H. Owen, D.F. Katz, A review of the physical and chemical properties of human semen and the formulation of a semen simulant, *J. Androl.* 26 (2005) 459–469, <https://doi.org/10.2164/jandrol.04104>.